Impoundment-associated Hydro-mechanical Changes and Regional Seismicity near the Xiluodu Reservoir, Southwestern China

Man Zhang[1, 3], Shemin Ge[2], Qiang Yang[1], and Xiaodong Ma[3]

[1] Tsinghua University, Department of Hydraulic Engineering, Beijing, China.

[2] University of Colorado, Department of Geological Sciences, Boulder, United States.

[3] ETH Zürich, Department of Earth Sciences, Zürich, Switzerland.

Corresponding author: Xiaodong Ma (xiama@ethz.ch)

Key Points:

- The plausible link between the Xiluodu reservoir impoundment and the increased seismicity is evidenced by spatio-temporal correlations.
- The pore pressure diffusion and reservoir water load can contribute to the fault reactivation and earthquake triggering in the Xiluodu area.
- The fault criticality analysis reveals that the NNW- and NS-striking faults downstream the Jinsha River are more prone to reactivation.

Abstract

Four large hydropower stations have recently been built downstream the Jinsha River in Southwestern China with a strong regional tectonic activity background. There is widely felt seismicity since the impoundment of the Xiluodu and Xiangjiaba reservoirs, increasing the public concern in this region. We begin with a criticality analysis of the faults near these reservoirs to quantify their susceptibility to triggered seismicity. Then we focus on the Xiluodu reservoir to investigate the correlation between the impoundment and seismicity nearby. We analyze the spatio-temporal distribution of seismicity near the Xiluodu reservoir, and identify the plausible rapid and delayed seismic response due to the impoundment. According to the impoundment record, we explicitly model the hydro-mechanical changes due to diffusion and reservoir water load, i.e., in pore pressure, elastic stress, and the resulting Coulomb stress. Our results show that the pore pressure changes can reach a level that may trigger fault reactivation and consequently, seismicity nearby. The water load can also induce the positive Coulomb stress changes on faults, depending on the fault orientation, which is especially important for understanding the earthquakes that occurred shortly after the impoundment and at more than 10 km distance from the reservoir. The combination of these two effects can induce positive Coulomb stress change over a larger area, which overlaps the majority of the events after the impoundment. While the causal relationship between the impoundment and seismicity warrants further analysis, we hope to inform the regional seismic impact of impoundment with this timely study.

1 Introduction

Four major hydropower stations (Wudongde, Baihetan, Xiluodu, and Xiangjiaba) have recently been built along the Jinsha River, Southwestern China (Figure 1). They all rank among the top five largest hydropower stations in China, with a total installed capacity of ~ 43 GigaWatt. The Xiangjiaba, Xiluodu, and Wudongde reservoirs have started the impoundment from December 2012, May 2013, and January 2020, respectively, and the impoundment of the Baihetan reservoir is scheduled for early 2021. Widely felt seismicity has been recorded since the initial operation of the Xiluodu (Diao et al., 2014; Duan, 2019; Luo et al., 2020) and Xiangjiaba (Yang et al., 2019) reservoirs, exhibiting spatio-temporal patterns that are plausibly related to the reservoir impoundment. The potential impact of reservoir impoundment on regional seismicity has received considerable attention and urgently demands a better understanding.

The influence of reservoir impoundment on seismicity is complex, depending on the reservoir operation, regional geologic and tectonic settings, and hydro-mechanical characteristics of rock masses (Gupta, 2002). Since the first case of Lake Mead in the late 1930's (Carder, 1945), there have been numerous reservoirs that are associated with triggered seismicity (El Hariri et al., 2010; Ge et al., 2009; Gupta, 1992, 2002; Lamontagne et al., 2006; Stabile et al., 2014; Zhang et al., 2018). The physical mechanisms of increased seismicity pertinent to reservoir impoundment have been extensively studied (Gupta, 1985; Ruiz-Barajas et al., 2019; Simpson, 1976; Talwani, 1997; Talwani & Acree, 1984), and generally can be attributed to the pore pressure diffusion and the reservoir gravitational loading (Bell & Nur, 1978; Simpson et al., 1988). Both correspond to the water level change during reservoir impoundment. The reservoir loading can change the elastic stress and induce instantaneous pore pressure change. The increase of pore pressure can reduce the effective stress on faults, and consequently their

resistance to shear slip. The elastic stress changes may either stabilize or destabilize the fault, depending on the fault orientation and the stress environment (Rajendran & Talwani, 1992; Segall & Lu, 2015). The collective impacts of pore pressure and elastic stress changes on fault reactivation are commonly considered to be primarily responsible for triggered seismicity, which can be quantified in terms of Coulomb stress changes (Harris, 1998; King et al., 1994). Previous studies suggest that Coulomb stress changes even of the order of 0.01 MPa can trigger seismicity on critically stressed faults (Cochran et al., 2004; Harris, 1998; King et al., 1994; Stein, 1999; Talwani, 2000).

This paper presents a case study of the Xiluodu reservoir, seeking to examine the plausible correlation between reservoir impoundment and regional seismicity. We first present the regional geomechanical setting near the four hydropower station sites downstream the Jinsha River. A fault criticality analysis is conducted as a first-order quantification of the faults' susceptibility to reactivation, considering the uncertainty of geomechanical parameters. Then, the earthquake catalog from May 2013 to January 2020 and water level records of the Xiluodu reservoir are analyzed to explore their spatio-temporal correlation. Subsequently, we simulate the evolution of pore pressure and elastic stress changes due to diffusion and water load, respectively, to yield estimations of the Coulomb stress changes at earthquake locations and relevant faults. With such, we hope to provide a useful and timely example to inform the possible impact of reservoir impoundment on the regional seismicity and its evolution, and offer a scientific perspective for the long-term operational decisions for these hydropower stations.

2 Geomechanical Setting and Fault Criticality

The Wudongde, Baihetan, Xiluodu, and Xiangjiaba dams are located to the east of the Sichuan-Yunan block (Figure 1(a)), which is the transitional zone between the eastern Tibetan Plateau and the Sichuan Basin (Xuan et al., 2016). The Sichuan-Yunan block is tectonically active (Pan & Shen, 2017) and belongs to the major North-South seismic zone in China (Wang et al., 2010). The maximum horizontal stress (S_{Hmax}) in the region, according to the World Stress Map (Heidbach et al., 2018; Heidbach et al., 2016; Hu et al., 2017), generally trends NW-SE, consistent with the regional tectonics and geodetic observations (Xu et al., 2016).

Fault systems are developed in this region. As shown in Figure 1(a), it primarily features NNW- to NS-striking faults, with fewer striking NE. Overall, the NNW- and NS-striking faults are associated with thrust faulting and a left-lateral strike-slip component, and the NE-striking faults dominantly exhibit thrust faulting with a right-lateral strike-slip component (Wen et al., 2013). The NNW-striking faults are present near the Wudongde and Baihetan dams, while no major faults appear near the Xiluodu and Xiangjiaba. Figure 1(a) shows that the historical earthquakes between 1936 and 2008 correlate well with these mapped faults, and as expected, the corresponding focal mechanism inversions are characteristic of thrust and strike-slip faulting. The upper crust is generally considered to be at or close to the state of frictional equilibrium (Zoback et al., 2002); therefore, (sub-)critically stressed faults could be reactivated due to small perturbations and cause seismicity (Raleigh et al., 1976; Robinson, 2004). The fact that most of the historical earthquakes were located along certain major faults in this region suggests that these faults are probably favorably oriented and thus critically stressed under the prevailing stress field.

There is a growing public concern about the increased seismicity following the impoundment of Xiluodu (Duan, 2019) and Xiangjiaba (Yang et al., 2019) reservoirs. The

potential seismic risk of the soon-to-be impounded Wudongde and Baihetan is also critical in the future. To assess the possibility of fault reactivation near these dams, we quantify the fault criticality, i.e., the proximity of faults to failure. We adopt the index of fault instability I proposed by Vavrycuk et al. (2013), which can be evaluated from the stress condition, fault frictional coefficient μ, and fault orientation (Section S1 in supporting information). (Hereafter, the Xiluodu, Baihetan, and Wudongde dams are abbreviated as XLD, BHT, and WDD, respectively.) The local stress conditions (i.e., principal stress directions and relative stress magnitudes) are derived via an iterative joint stress inversion (Vavrycuk, 2014) from focal mechanisms in each area. The Xiangjiaba area is not included in the stress inversion due to insufficient focal mechanisms. The inverted stress state in the XLD area is dominated by thrust faulting and transitioning into strike-slip, and the stress state in the BHT and WDD area is dominated by strike-slip and transitioning into thrust faulting, suggesting a spatial variation of the in-situ stress field (Table S1 in Supporting Information). This is relatively consistent with the regional tectonic stress state (Cui et al., 2006; Tian et al., 2019).

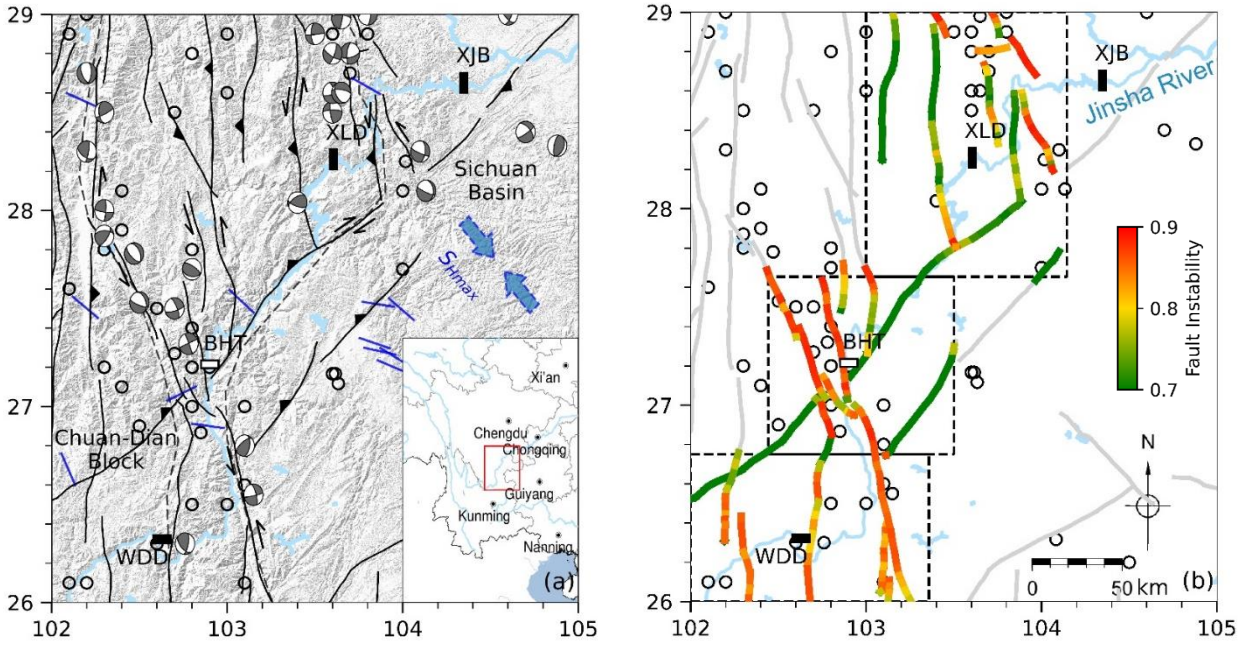

Figure 1. (a) Faults and M3+ earthquakes (circles and/or beach balls) between 1936 and 2008 downstream of the Jinsha River in southwestern China. Blue lines denote the azimuth of the maximum horizontal stress obtained from the World Stress Map. Blue arrows show the orientation of regional horizontal compression from reference (Xu et al., 2016). Dashed lines show the block boundary. (b) Fault map with quantified fault criticality in areas of Wudongde, Baihetan, and Xiluodu reservoirs (WDD, BHT, and XLD). Fault segments therein are colored by an area-weighted average of fault instability. Fault segments colored red represent $I_m \geq 0.9$; those in green represent $I_m \leq 0.7$. Black rectangles show the locations of four dams. Light blue represents rivers and lakes.

The spatially varying stress field warrants the analysis of each area individually. Acknowledging the uncertainty and natural variability of the geomechanical parameters in evaluating the fault instability I, we follow the approach by Walsh & Zoback (2016) with the Monte Carlo method. We assign reasonable distributions of each parameter and simulate various

scenarios on each fault segment. We solve the probability of the fault instability *I* at 5 km depth (where most seismicity in the Xiluodu area occurred, as detailed in Section 3). The fault criticality analysis is elaborated in Supporting Information S1.

Figure 1(b) presents the resolved criticality of each fault segment by their corresponding I_m, in a color-coded fashion, with red representing less stable and green more stable. I_m represents the area-weighted average of 10,000 results of fault instability *I* of Monte Carlo simulation. The fault segments that are colored red correspond to $I_m \geq 0.9$, and those in green represent $I_m \leq 0.7$. As shown in Figure 1(b), the majority of the red-colored fault segments are NNW- and NS-striking, especially near the WDD and BHT, and the NE-striking faults are almost all colored green in these three areas. In the XLD area, the NS-striking faults are generally green-colored, albeit with some orange to red segments; the NNW-striking faults are primarily red-colored. It appears that the NNW- and NS-striking faults near the BHT and WDD reservoirs, in the transitional strike-slip and/or thrust faulting stress environment, are more prone to reactivation than those near the XLD reservoir, which is dominated by thrust faulting stress environment. Such heterogeneity in the criticality of sub-parallel faults could be attributed to the spatial variations of the stress field.

The orientations of inverted maximum principal stresses in each area are generally sub-horizontal. However, the departure of the inverted minimum and/or intermediate principal stresses from being vertical is of questionable importance (Table S1). This deviates from the classical assumption, i.e., one of the principal stresses is perpendicular to the Earth's surface (Zoback, 2007). Two factors can contribute to these deviations. One is the insufficient focal mechanism solutions used in stress inversion, which might lead to biased local stress state only characteristic of the resolved events. The other is the complexity of regional tectonics, especially for the Sichuan-Yunan block and its adjacent areas (Jin et al., 2019), which can induce spatial rotation and variation of the stress field. To incorporate these stress inversion uncertainties, we also evaluate the fault criticality for two extreme cases of the stress environment, thrust and strike-slip faulting, i.e., assuming the overburden stress to be the minimum and intermediate principal stress, respectively (see Supporting Information S1). As shown in Figure S3, the faults become systematically more critical in the strike-slip faulting environment, consistent with the results shown in Figure 1(b). The relative fault criticality underscores that the NNW- and NS-striking faults in these reservoir regions have a higher probability of being reactivated than those that are NE-striking. Therefore, this observation suggests more attention should be paid to the seismic risk associated with the former.

It is noted that most historical M3+ earthquakes correlate well with the distribution of the red- and orange-colored NNW- and NS-striking faults. This correlation corroborates the primary control of fault criticality on seismicity occurrence, but there remain some obstacles to predict the regional seismicity evolution. The fault criticality is a conditional scalar index based on the assumed probabilistic distributions of in-situ stress field, fault geometry, and frictional coefficient, which are quite heterogeneous and difficult to constrain (Shen et al., 2019; Snee & Zoback, 2018; Walsh & Zoback, 2016). Despite the possible deviation of the assumed parameter distributions from the realistic in-situ conditions, the first-order quantification of fault criticality is rather informative to estimate the faults' susceptibility to reactivation, particularly in the context of nearby reservoir impoundment.

3 Xiluodu Impoundment History and Seismicity

Xiluodu is currently the third-largest hydropower station in the world, second in China. The Xiluodu dam is a double-curved arch dam with a crest elevation of 610 m and a height of 285.5 m. It situates in the Leibo-Yongshan tectonic basin, surrounded by the Ebian-Jinyang fault (EJF), Huayingshan-Lianfeng fault (HLF), and Mabian-Yanjin fault zone (MYF, composed of several sub-parallel faults) (Figure 2). The Jinhekou-Meigu fault (JMF) is sub-parallel to and to the west of the EJF. The Xiluodu reservoir is a typical river-type reservoir with a surface impoundment extension of ~ 204 km along the Jinsha River (Yin et al., 2015), and intersects the EJF and HLF upstream. The minimum distance between the Xiluodu reservoir and the MYF and the JMF is ~ 10 km and ~ 30 km, respectively.

The impoundment process of the Xiluodu reservoir can be generally divided into three stages (Figure 3). In the first impoundment period (P1), from May 2013 to May 2014, the water level elevation quickly rose from 440 to 542 m within the first ~50 days with a maximum water level change of 120 m. The second impoundment period is the first storage cycle (P2). Starting on May 20, 2014, the water level increased from 540 m to its historical high of 600 m on September 28, 2014. After ~6 months, the water level gradually decreased to 545 m in June 2015. Then the third impoundment period (P3) continues to the present (data is collected until the end of 2019 in this study). The reservoir water level undergoes yearly seasonal variations between the maximum water levels during the rainy season and minimum during the dry season (Figure 3(a)). The Xiluodu reservoir has experienced six filling and five drawdown processes between May 2014 and January 2020.

Felt earthquakes near the Xiluodu dam (XLD) were rare before the impoundment. However, a significant increase of seismicity was recorded in the XLD area following the impoundment, including an M5.1 and an M5.2 event on April 5, 2014, and August 17, 2014, respectively. The temporal and spatial patterns of M1+ earthquakes in the XLD area following the impoundment are shown in Figure 2 and Figure 3, respectively. Most earthquakes concentrated within a 30 km by 20 km area near the dam, and the other events clustered near the surrounding faults. To better quantify the spatio-temporal features of seismicity, we arbitrarily define five regions, R1 to R5, according to the distribution of seismicity (see Figure 2).

Most post-impoundment seismicity occurred in Region 1 (R1); in contrast, there are only five M1+ earthquakes with a maximum magnitude of 1.8 recorded within four years prior to the impoundment (Figure 3 (c)). A burst of small earthquakes occurred at the beginning of impoundment in May 2013, which we categorize as ‘rapid response’ to the water level change and might be related to the elastic loading and coupled pore pressure changes (Simpson et al., 1988). The second impoundment period (P2) is quite seismically active, including approximately half of the R1 events following the impoundment. The month that M1+ earthquakes hiked to their maximum number (≈ 55) coincides with the historical highest water level change (Figure 3). During the third impoundment period (P3), the monthly seismicity rate declined significantly compared to that in P2, fluctuated and generally reached its yearly peak between May to October. As shown in Figure 3(a-d), in R1, there are approximately 440 M1+ earthquakes recorded during these three impoundment periods; about two-thirds of events are below M2. Most of these events are within 10 km depth and concentrate within 5 km depth. We also notice that the events gradually migrated further from the reservoir (Figure 2(a)), and both the monthly seismicity rate and maximum magnitude of earthquakes in R1 continuously increased after 2015 (Figure 3 (c)), including an M 4.7 event on May 26, 2019. These earthquakes with a significant

delay after the initial impoundment, as well as their further distance from the reservoir, generally can be identified as 'delayed response' and might be attributed to pore pressure diffusion (Simpson et al., 1988).

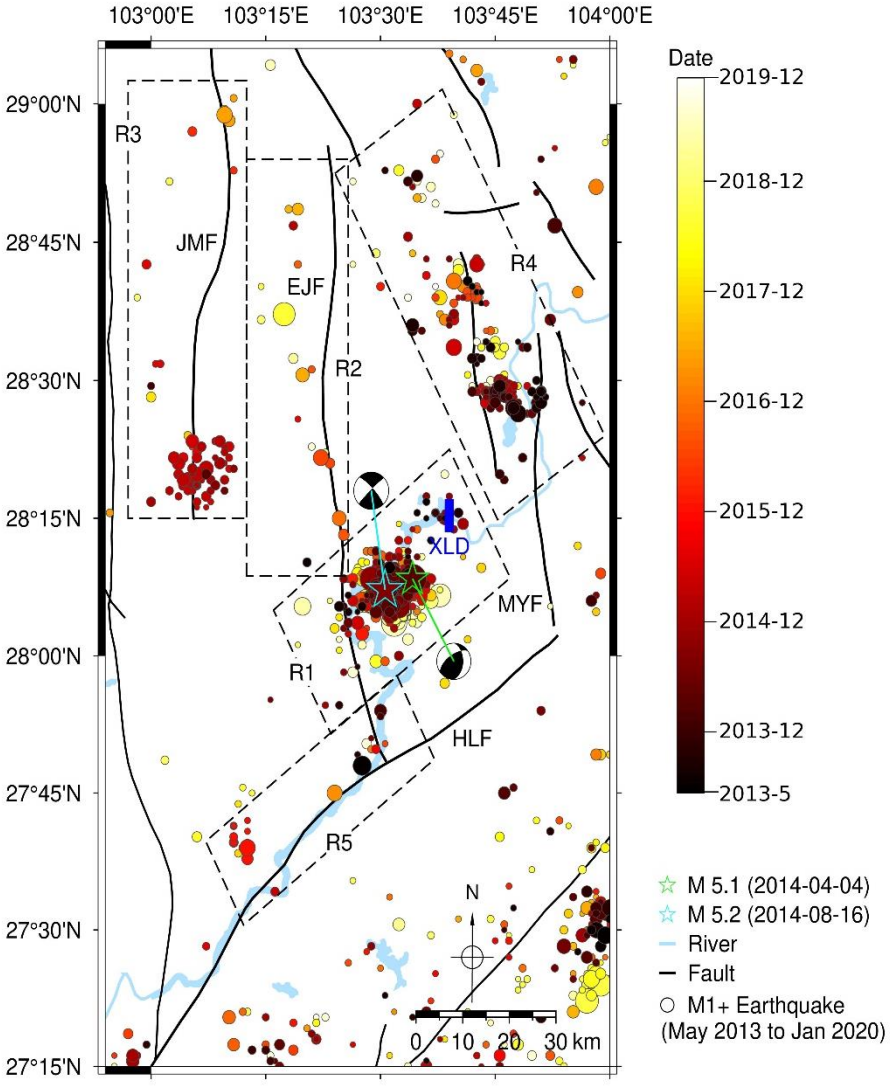

Figure 2. Mapview of M1+ earthquakes observed in the XLD area from May 2013 to January 2020. The subregions R1 to R5 (dashed boxes) are arbitrarily defined according to the spatial seismicity distributions.

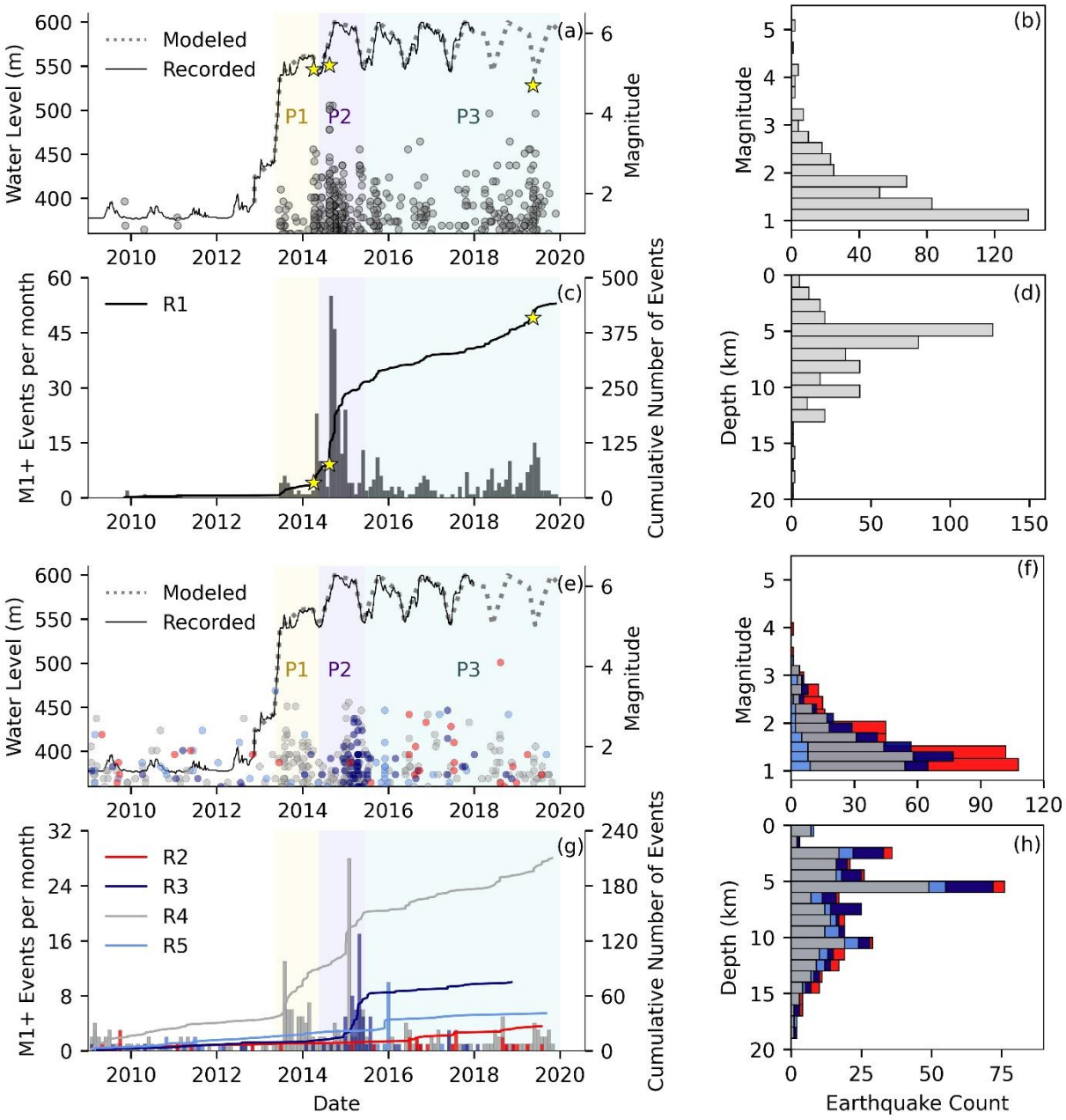

Figure 3. Evolution and statistics of M1+ seismicity in each sub-region: (a-d) R1 and (e-h) R2-R5 (defined in Figure 2). Yellow stars represent M4.5+ earthquakes. The observed and modeled (see Section 3) water level changes are represented by the solid and dashed line, respectively. The three periods named P1, P2, and P3 refer to the three periods following the impoundment.

The seismicity is also statistically analyzed in the other four regions, R2 to R5, corresponding to the four major fault zones shown in Figure 3(e-h). As shown in Figure 3, the seismicity following the impoundment in those four regions has also experienced rapid increase and plateau; however, with temporal and spatial variations from one to another. The seismicity distribution near the EJF in R2 suggests an along-fault propagation, with the occurrence of a maximum magnitude of 4.1 in August 2018. In R3, the seismicity rate sharply increased after the

water level change reached its maximum value of 160 m (corresponding to the water level of 600 m), and most earthquakes are located near the southern end of the JMF, with a maximum magnitude of 1.8. In R4, the events burst almost instantaneously with the initial impoundment from May 2013 and continued through the first impoundment period (P1); the maximum seismicity rate was reached when the water level attained its historical high in P2, and then the events continued at a moderate rate thereafter (P3). The seismicity in R5 migrates further upstream the reservoir, with a maximum magnitude of 3.4 taking place at the very beginning of the impoundment. These observations of both rapid and delayed seismic response to reservoir water changes suggest that the seismicity near the faults are very likely to be associated with the Xiluodu reservoir impoundment. It appears that the seismicity rate change in R4, unlike R2, R3, and R5, follows a similar trend to that of R1 (more visible on their cumulative statistics). A possible explanation for this might be that the MYF in R4 is located downstream the Xiluodu reservoir and upstream the Xiangjiaba reservoir, and the impoundment of the latter can also contribute to R4 seismicity effectively. In the absence of Xiangjiaba data, we do not verify this hypothesis in this study.

Duan (2019) resolved that the focal mechanism solutions of earthquakes near the head area of the Xiluodu reservoir following the impoundment are mainly the combination of thrust and strike-slip faulting, while the focal mechanism solutions of earthquakes near the EJF and MYF are dominated by thrust faulting and strike-slip faulting, respectively. This observation is consistent with the faulting styles and the inverted stress field in this area, further suggesting a relatively clear correlation between these major faults and nearby earthquakes.

In short, a plausible link between the increased seismicity and reservoir impoundment in the XLD area is evidenced by both spatial and temporal correlations. Dissimilar seismicity response between different sub-regions (R1-R5), from rapid to delayed seismic response to reservoir water level changes, and the different characteristics of seismicity frequency and magnitude therein, might be related to the complex interaction between water load and pore pressure diffusion (Simpson et al., 1988). The understanding of the hydro-mechanical impact of reservoir impoundment on increased seismicity is therefore needed for correlating with the evolution of regional seismicity.

4 Pore Pressure Diffusion due to Impoundment

4.1 Method and Modeling

To quantify the pore pressure diffusion due to the Xiluodu reservoir impoundment, we utilize MODFLOW, a finite-difference groundwater flow code. It can simulate the three-dimensional transient groundwater flow through anisotropic and heterogeneous porous media by solving the following 3-D transient groundwater flow equation for the hydraulic head (Harbaugh, 2005; Harbaugh et al., 2017):

$$S_s \frac{\partial h}{\partial t} = \frac{\partial}{\partial x}\left(K_x \frac{\partial h}{\partial x}\right) + \frac{\partial}{\partial y}\left(K_y \frac{\partial h}{\partial y}\right) + \frac{\partial}{\partial z}\left(K_z \frac{\partial h}{\partial z}\right) + Q \quad (1)$$

where h is the hydraulic head (m), K is hydraulic conductivity (m s^{-1}, in x, y, and z directions) and S_s is specific storage (m^{-1}), Q is fluid source rate (m^3 s^{-1}). The ratio of K and S_s is hydraulic diffusivity D (m^2 s^{-1}). Pore pressure change (ΔP) can be obtained by $\Delta P = \gamma \Delta h$, where γ is the specific weight of water (N m^{-3}), and Δh is the change of hydraulic head.

The modeled area that encompasses the entire XLD area is shown in Figure 2. To minimize the model boundary effect on the pore pressure diffusion, the model domain is expanded to 148 km (east-west) by 248 km (north-south) by 30 km (depth), with more than 1.6 million gridded cells (Figure 4). We restrict the vertical presence of all faults to be 15 km, which is the limiting depth that most earthquakes are located. We assume the fault dip angles to be 60º for the EJF, HLF, and JMF, 90º for the MYF, the reasonable values available from limited references (Cui et al., 2019). We assign a changing head boundary on the grids corresponding to the location of the reservoir to simulate the impoundment process. The recorded water level variations at the dam are simplified and extended as the model input, i.e., six filling and five drawdown processes, as shown in Figure 3(a). We assume that the change of water level due to impoundment linearly decreases further upstream from the dam. The four side boundaries of the model domain are set to zero head changes since the reservoir is distant enough. In short, we assume that the pore pressure changes are due to reservoir impoundment only. We focus on the modeled pore pressure changes at the hypocenters of M1+ earthquakes in R1 to R5. We also emphasize the pore pressure evolution at 5 km depth at six typical locations on the known faults and one location underneath the head area of the Xiluodu reservoir (Figure 4), where most of the earthquakes are located.

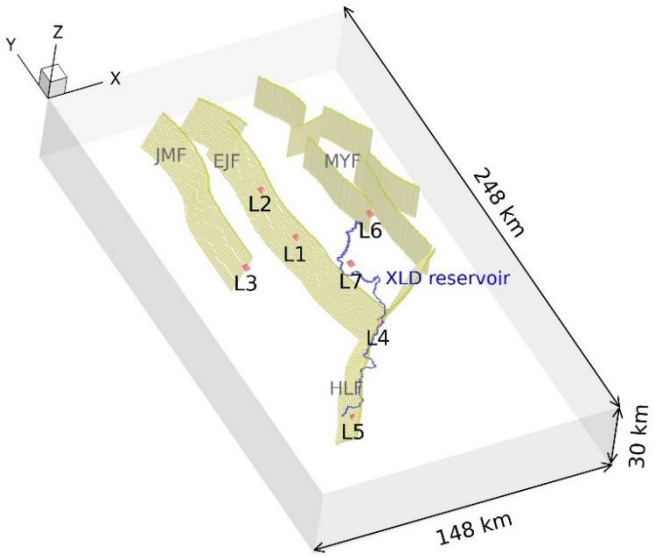

Figure 4. 3D numerical model domain for pore pressure diffusion simulation. The modeled Xiluodu reservoir are in blue and faults in yellow. Red dots represent pore pressure monitoring locations on faults at 5 km depth.

The hydrologic parameters of the pore pressure diffusion model include hydraulic conductivity K, specific storage S_s, and hydraulic diffusivity D expressed as the ratio of K/S_s, which mainly depends on the lithology and geological structure of the rock masses. According to previous studies, the hydraulic diffusivity values beneath the reservoirs generally vary between 0.1 and 10 $m^2\ s^{-1}$ (Talwani et al., 2007). We resolve the possible range of equivalent hydraulic diffusivity in the rock masses beneath the Xiluodu reservoir between 0.32 and 4.6 $m^2\ s^{-1}$ (Figure S4 in supporting information), assuming that the M1+ earthquakes in R1 are due to diffusion of elevated pore pressure. It should be noted that the hydraulic diffusivity estimated under this assumption might contain various uncertainties and tend to be overestimated (Ge et al., 2009;

Talwani & Acree, 1984), and the actual hydraulic diffusivity can range several orders of magnitude. In the absence of direct measurement of hydraulic diffusivity in the study area, we adopt several possible values of the hydraulic diffusivity for basement rock within 15 km depth (D_r = 0.05, 0.5, and 2 m^2 s^{-1}) and for high-diffusivity fault zones (D_f = 1, 5, and 10 m^2 s^{-1}), to allow for possible ranges of estimated pore pressure perturbations.

Table 1 presents the five modeling cases with different combinations of basement and fault zone hydraulic diffusivity. In all cases, the hydraulic diffusivity in the basement rock below 15 km is set to 0.001 m^2 s^{-1}. The specific storage S_s is generally assumed to be between 10^{-5} and 10^{-7} m^{-1} for pore pressure diffusion modeling (Brown et al., 2017; Ortiz et al., 2019; Pandey & Chadha, 2003; Wetzler et al., 2019; Yeo et al., 2020; Zhang et al., 2013). Here, we assign a constant specific storage S_s of 5×10^{-7} m^{-1} to basement rock and 10^{-5} m^{-1} to fault zones in all scenarios.

Table 1. List of Hydraulic Diffusivity Values for Basement Rock (D_r) and Fault Zones (D_f).

Case	Diffusivity (m^2 s^{-1})	
	D_r, Basement (depth ≤ 15 km)	D_f, Fault
A	0.05	5
B	0.5	5
C	2	5
D	0.5	1
E	0.5	10

4.2 Spatio-temporal pore pressure diffusion

The simulated spatial extent of pore pressure change expands with time since the impoundment, basically following the geometry of the reservoir. Figure 5 shows the spatial distribution of the modeled ΔP for Case B, the moderate combination of hydraulic diffusivities, D_r ~ 0.5 m^2 s^{-1} and D_f ~ 5 m^2 s^{-1}, in plain view and cross sections of faults (see Figures S5-S8 for other cases). Two temporal snapshots are presented, one in October 2014, the first time when the reservoir water level reached its maximum value and the maximum seismicity rate observed, and one in January 2020. In the reservoir head area at 5 km depth, where most of the seismicity occurred following the impoundment, the lateral extent of influence where $\Delta P \geq 0.01$ MPa is within 30 km of the reservoir in October 2014 and can increase to nearly 60 km in January 2020. The maximum values of ΔP can reach 0.2 MPa in October 2014, and further increase to over 0.5 MPa in January 2020. Case A and Case C represent the lower and an upper limit for the simulated pore pressure change, respectively. For lower diffusivity value (D_r ~ 0.05 m^2 s^{-1}, Case A), the pore pressure perturbation is significantly smaller and mainly dominated by the EJF and HLF, extending to further distance but at shallower depth over time along these two faults than Case B (Figure S5). As anticipated, for higher diffusivity value (D_r ~ 2 m^2 s^{-1}, Case C), the pore pressure diffusion is very significant, and the extent of influence where $\Delta P \geq 0.01$ MPa is over 50 km in October 2014 and can reach the JMF and MYF in January 2020 (Figure S6).

We also explored the effect of the impoundment on high-diffusivity fault zones, which can channel the pore pressure diffusion over large distances and lead to the localized pore pressure increase. The intersections between faults and the reservoir can quickly respond to the water level change and act as the main conduits of diffusion along the faults. However, the pore

pressure diffusion is less likely to reach the faults without the direct hydraulic connection with the reservoir. For Case B of D_f ~ 5 m^2 s^{-1}, the extent where $\Delta P \geq 0.01$ MPa increases over 30 km along the EJF between October 2014 and January 2020; the modeled pore pressure appears to permeate throughout the entire HLF in January 2020, while the pore pressure changes on the JMF and MYF are still negligible. For lower diffusivity values of D_f ~ 1 m^2 s^{-1} (Case D), the ΔP along the faults are not distinguishable from that in the basement rock, and the ΔP tends to only build up underneath the head area of the reservoir (Figure S7). As expected, a higher diffusivity value (D_f ~ 10 m^2 s^{-1}, Case E) can significantly facilitate pore pressure diffusion, and the extent where $\Delta P \geq 0.01$ MPa can extend further along the EJF and reach the southern end of MYF in January 2020 (Figure S8).

We further quantify the pore pressure evolution more specifically at seven 'virtual' monitoring locations, i.e., six on-fault (L1 to L6) and one in R1 (L7) at 5 km depth (Figure 4). Figure 6 shows the simulated pore pressure changes over time at these monitoring locations for Case B. With the water level change, the pore pressure changes at L4 and L7, both are directly underneath the reservoir, significantly increase over time. The ΔP at other monitoring locations gradually builds up at a relatively lower rate over time. Till January 2020, the pore pressure changes of L1 and L5 are nearly 0.1 MPa, while the ΔP of L2, L3, and L6 are not measurable. The results of other case studies confirm that the increase of both D_r and D_f can promote pore pressure change at these monitoring locations (Figure S9). The time that ΔP reaches 0.01 MPa at L3 is predicted to be January 2019, December 2017, and January 2017 for Case A, C, and D, respectively. We note that the ΔP at L3 can only exceed 0.01 MPa at the end of 2017 with D_r ~ 2 m^2 s^{-1} (Case C) in our study, suggesting that significant pore pressure perturbations along JMF are unlikely.

The above results indicate that higher hydraulic diffusivity of both the rock masses and fault zones can promote the propagation of pore pressure front, increasing its possibility of reaching the critically-stressed faults and triggering slip. It is worth noting that we simplify the hydraulic diffusivity to be isotropic and constant in the model, without considering its spatial variations (Ingebritsen & Manning, 1999) and the pressure dependence of hydraulic diffusivity (Gao et al., 2020; Gavrilenko & Gueguen, 1989; Heller et al., 2014). Moreover, the possible existence of some hydraulically-conductive unmapped faults can further the pore pressure diffusion process. That said, our modeling results highlight the significant contribution of the impoundment to pore pressure change in the rock masses underneath the reservoir, and the channeling effects of high-diffusivity fault zones on pore pressure diffusion. Particularly in the head area of the reservoir, pore pressure diffusion is considerable with $D_r \geq 0.5$ m^2 s^{-1} and seems to overlay the extent where most earthquakes are located following the impoundment. The pore pressure diffusion along the EJF and HLF, which intersect with the reservoir, is extensive even for the lower limit of pore pressure changes (Case A); therefore, these two faults and the regions nearby are expected to be more prone to reactivation after the impoundment. However, the impoundment process has limited influence on pore pressure changes near the MYF and JMF because of their relatively larger distance to the reservoir.

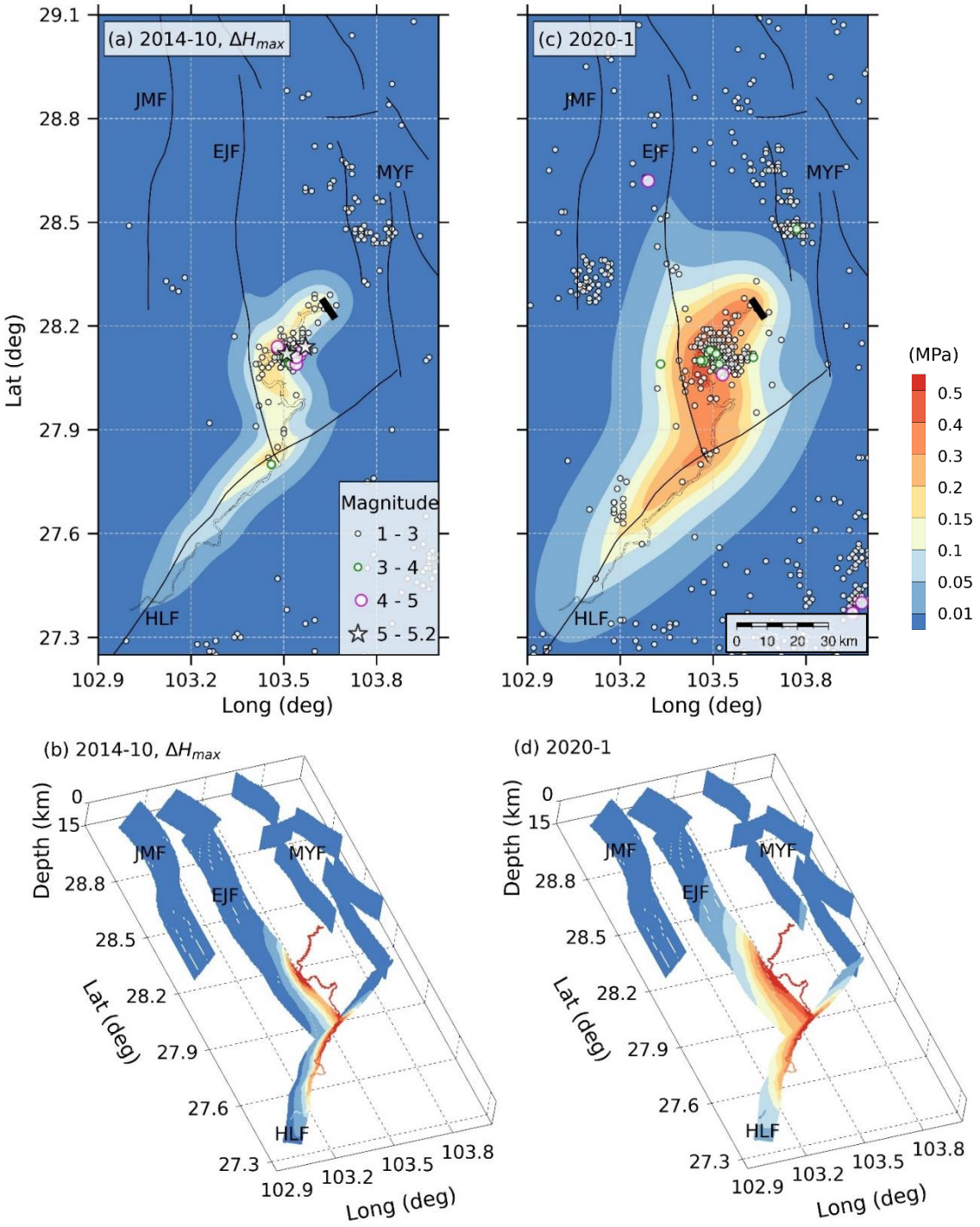

Figure 5. Spatial evolution of pore pressure changes for Case B. Pore pressure distribution at 5 km depth on (a) October 10, 2014, for the first time when the water level change reached its maximum value, i.e., ΔH_{max} = 160 m and (c) January 1, 2020. Pore pressure diffusion on fault on (b) October 10, 2014, and (d) January 1, 2020. The M1+ events recorded between May 2013 and October 2014 and between November 2014 and January 2020 are shown in (a) and (c), respectively.

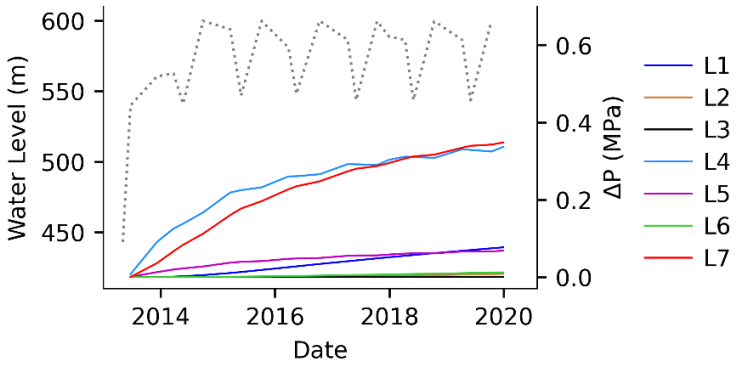

Figure 6. Pore pressure changes (ΔP) at seven pore pressure monitoring locations (L1-L7) at 5 km depth following the impoundment of Xiluodu reservoir for Case B.

4.3 Correlation between Pore Pressure Changes and Seismicity

The seismicity following the impoundment tends to migrate away from the Xiluodu reservoir over time, coinciding with the expanding pattern of pore pressure diffusion. For Case B, as shown in Figure 5(a) and (b), the M1+ events between May 2013 and October 2014 mainly cluster within an elongated narrow zone beneath the head of the reservoir. From October 2014 to January 2020, according to our model, the area of elevated pore pressure significantly expanded, which seems to encompass the area where produced much of the seismicity during this period. Figure 7 further presents the ΔP when the M1+ events occurred in each region for Case B, and see Figures S10-S13 for other cases. As expected, the ΔP at the hypocenters of M1+ events in R1 and R5 significantly increases, even for the events that occurred shortly after the impoundment, due to their short distances to the reservoir. The median pore pressure changes in R1 significantly increase with D_r and reach values between 0.01 and 0.27 MPa (Figure 8). Indeed, for ~16.7% of the M1+ events in R1, the ΔP at their hypocenters can exceed 0.01 MPa, the threshold generally referred to for triggering seismicity on critically stressed faults (King et al., 1994; Reasenberg & Simpson, 1992), for Case A; while over 92% for the other four cases (Figure 8). The ΔP of the M4.7+ events on May 2019 beneath the head area of the reservoir, which could be related to the delayed seismic response to impoundment as discussed in Section 2, can reach the value of approximately 0.002 MPa for Case A, and increase to over 0.2 MPa for other cases. It is noted that the modeled ΔP at some hypocenters in R2 can also exceed 0.01 MPa, and increase with D_r and D_f. Thus, we can first conclude that most earthquakes near the reservoir, and the along-fault migration of seismicity near EJF have a great chance to be directly triggered by pore pressure diffusion.

The pore pressure changes at some hypocenters, especially those at greater depths and further distances, are not significant when those events occurred. For all the cases modeled in this study, the modeled ΔP of the M5.1 earthquake can range between 0.0003 to 0.022 MPa; however, the ΔP of the M5.2 earthquake is always negligible for all cases (Figure 7, and Figure S10 to S13). This is due to that the M5.2 event is located at 21.6 km depth, which is practically too deep for pore pressure diffusion to reach at the time of the event. Moreover, there is also no significant increase of ΔP for some other events, especially for events in R3 and R4. With D_r~ 0.5 m2 s-1 (Case B), the ΔP of events in R4 is negligible during P1 and P2, and tends to increase only after 2017, while the ΔP of events in R3 is practically zero. Even with D_r~2 m2 s-1 (Case

C), the upper bound of pore pressure diffusion in this study, the ΔP of events in R3 and R4 only slightly increases and generally are smaller than 0.005 MPa. There are several possible explanations for the result that modeled pore pressure changes are not significant at these hypocenters. Neither the precise locations of most events nor reliable fault orientations at depths are available in this study. However, we have noted that the relative location of faults and reservoir can strongly influence the modeled pore pressure changes at earthquake hypocenters, especially for those events which are far from the reservoir and are sensitive to the channeling effect of high-diffusivity faults. Therefore, we might underestimate or overestimate the pore pressure changes at some hypocenters located on or near the JMF and MYF. Alternative mechanisms can also be relevant to the earthquake triggering, including the water-weakening effects on fault strength (Masuda et al., 2012) and the far-field poroelastic effect due to water load (Goebel et al., 2017; Guglielmi et al., 2015; Segall et al., 1994).

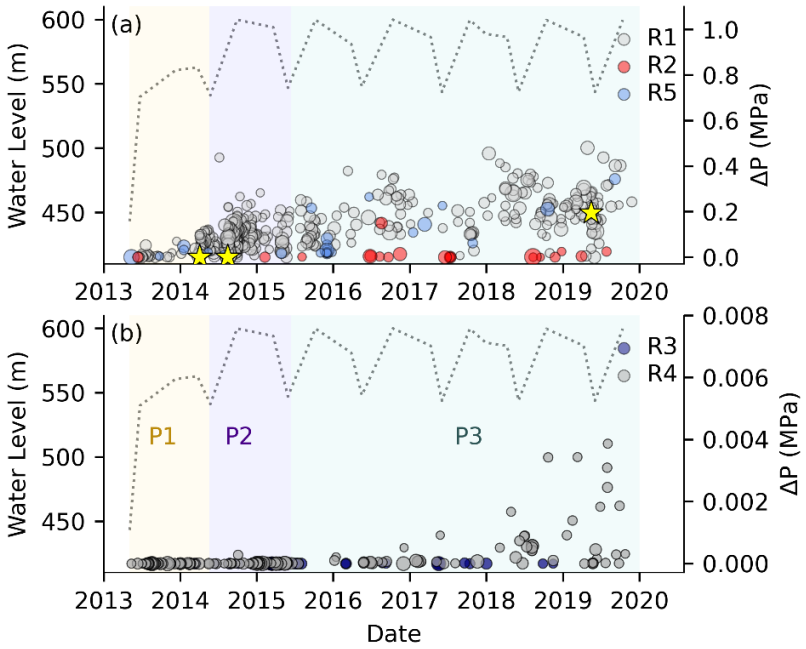

Figure 7. Modeled pore pressure changes **(**ΔP) at the time and location of occurred earthquakes in each region for Case C. Yellow stars represent M4.5+ earthquakes.

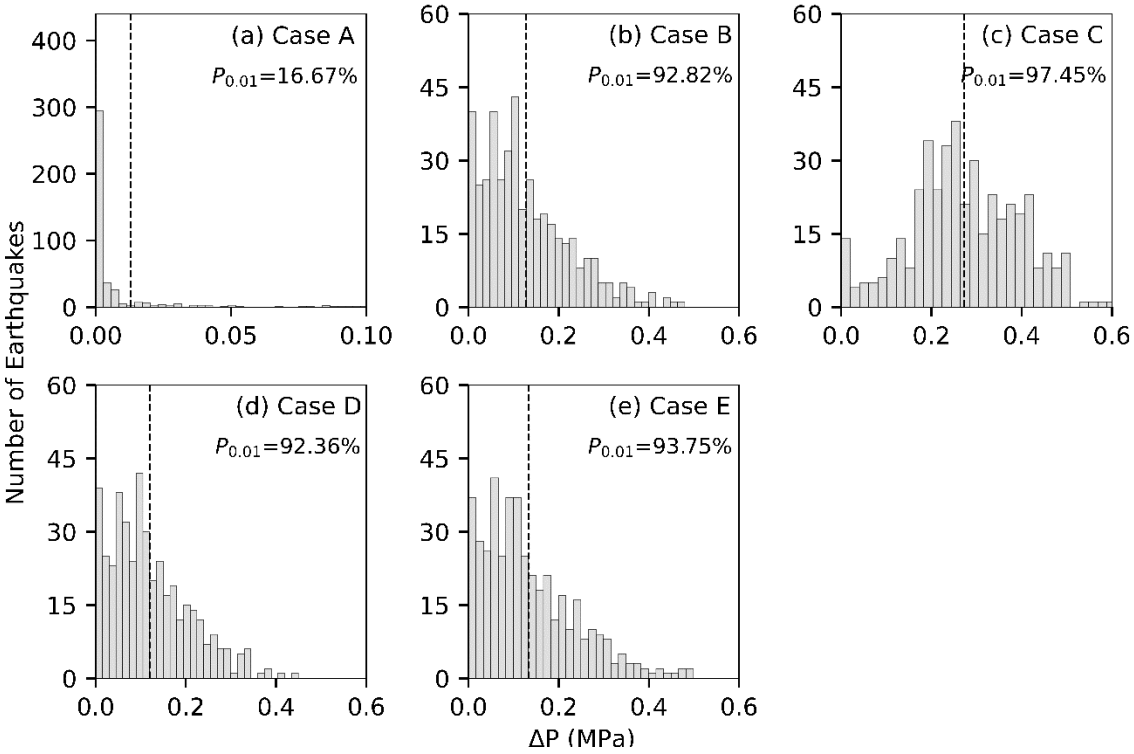

Figure 8. Distribution of the modeled pore pressure changes (ΔP) at the event hypocenters following the impoundment of the Xiluodu reservoir in subregion R1 for each modeling case. The dashed line indicates the median of the distribution. $P_{0.01}$ is the percentage of events with pore pressure changes exceeding 0.01 MPa.

5 Coulomb Stress Changes

5.1 Method and Modeling

The simulation of elastic stress changes due to reservoir water load is performed using the finite-difference code FLAC3D (Itasca, 2012). The stress model domain is the same as that in the pore pressure diffusion modeling. We employ a linear elastic and isotropic material to represent the crustal rock masses, albeit being simplistic. The assigned Young's modulus and shear modulus are 37.5 GPa and 15 GPa, respectively, for the crust (Tao et al., 2015), and 3.75 GPa and 1.5 GPa, respectively, for the fault zones. The modeled upstream water level change is also set to to decrease with distance from the dam linearly, and the modeled stress changes are due to reservoir impoundment only. Here, we assess the effective Coulomb stress change (ΔCFS) in the context of decoupled linear poroelasticity (Biot, 1956; Cheng, 2016; Cocco & Rice, 2002; Roeloffs, 1988). The effective Coulomb stress change (ΔCFS_{eff}) in terms of the mechanical effect and hydrologic effect is defined as (Ge et al., 2009):

$$\Delta CFS_{eff} = \Delta\tau - \mu\Delta\sigma_n + \mu\Delta P_u + \mu\Delta P_d \quad (2)$$

where $\Delta\tau$ and $\Delta\sigma_n$ are the shear stress (along the slip direction) and normal stress changes on the fault, respectively (compression-positive); ΔP_u is the undrained pore pressure, which can build up instantly due to the water load. ΔP_d is the diffused pore pressure. If assuming $\Delta P_u =$

$B\Delta\sigma_n$, with B being the Skempton coefficient that varies between 0 and 1 with rock type, Equation (2) becomes:

$$\Delta CFS_{eff} = \Delta\tau - \mu(1-B)\Delta\sigma_n + \mu\Delta P_d = (\Delta\tau - \mu'\Delta\sigma_n) + \mu\Delta P_d = \Delta CFS_s + \Delta CFS_p \quad (3)$$

where $\mu' = \mu(1-B)$ is the effective (or apparent) friction coefficient (Cocco & Rice, 2002; Harris, 1998). ΔP_u is at its maximum value upon loading without diffusion to occur, and dissipates with the diffusion process and deformation of rock masses over time. ΔCFS_s and ΔCFS_p are the induced Coulomb stress changes resulting from reservoir loading and pore pressure diffusion, respectively. We assume μ'= 0.14, with μ = 0.71 and B = 0.8, to estimate the Coulomb stress changes resulting from the water load. This represents a reasonable upper bound of ΔCFS_s under undrained conditions with a given water load, assuming that the rock underneath the reservoir is saturated before the reservoir impoundment. It is worth noting that the ΔCFS_{eff} defined in Equations (2) and (3) involves the coupled process of pore pressure diffusion and stress changes due to water load, referring to poroelastic effects (Cheng, 2016). However, the numerical simulation of stress changes in this study is static and decoupled from the process of pore pressure diffusion. The neglected effect of the dissipation of undrained pore pressure may lead to the overestimation of ΔCFS_{eff}, if the pore pressure diffusion has already taken place. Thus, we quantified the Coulomb stress changes induced by the reservoir load and pore pressure diffusion separately, without superimposing the ΔCFS_s and ΔCFS_p directly to obtain the distribution of ΔCFS_{eff} throughout the study area.

5.2 Coulomb Stress Changes at the Hypocenters of Two M5+ earthquakes

We first calculate the Coulomb stress changes at the hypocenters of the M5.1 and M5.2 earthquakes to quantify the seismogenic impact of the reservoir impoundment. The water level changes at the time of both events were about 100 m. The focal mechanism solutions of these two events are obtained from ISC's Seismological Dataset Repository; however, the faulting planes are not distinguished from the auxiliary planes. Thus, the stress changes are calculated for both nodal planes. As shown in Table 2, the positive ΔCFS_s on both nodal planes of the M5.1 event favors the triggering effect of reservoir load, while the negative ΔCFS_s of the M5.2 event stabilizes the fault. This is because the $\Delta\tau$ induced by water load is positive for the M5.1 event but negative for the M5.2 event, mainly depending on their depths. Taking into account the pore pressure diffusion, we expect that the ΔCFS_{eff} of the M5.1 event can be close to 0.01 MPa, which is generally considered to be of relevant significance in triggered seismicity on critically stressed faults. In contrast, the ΔCFS_{eff} of the M5.2 event is still negative.

These results suggest that stress changes induced solely by reservoir load can plausibly trigger the M5.1 event, and pore pressure diffusion also tends to promote the occurrence of this event. Although the poroelastic effect has been widely accounted for to explain triggered seismicity at great depths and distances (Goebel et al., 2017; Guglielmi et al., 2015; Segall et al., 1994), the modeled stress changes due to the combined effects of reservoir load and pore pressure diffusion do not favor the occurrence of the M5.2 event. Alternative mechanisms can plausibly be relevant, e.g., Coulomb stress transfer (King et al., 1994; Stein, 1999), which may destabilize faults in affected areas and subsequently trigger larger events (Brown & Ge, 2018; Sumy et al., 2014; Yeo et al., 2020). We notice that many smaller earthquakes occurred close to the M5.1 and M5.2 events, both temporally and spatially (Figures 2 and 3(a)). Thus, the

cumulative effect of Coulomb stress transfer induced by previous smaller events can potentially be responsible for the occurrence of these two M5+ events.

Table 2. Focal mechanism solutions of two M5+ events, the modeled elastic stress, pore pressure (for Case B), and Coulomb stress changes corresponding to the water level change ΔH = 100 m, with μ = 0.71 and B = 0.8.

Date	Depth (km)	ML / Mw	Nodal Plane	Strike / Dip / Rake (º)	$\Delta\tau$ (MPa)	$\Delta\sigma_n$ (MPa)	ΔCFS_s (MPa)	ΔP (MPa)	ΔCFS_{eff} (MPa)
2014-04-04	12.4	5.1 / 4.9	1	235 / 60 / 125	0.011	0.009	0.010	0.0003	0.010
			2	360 / 45 / 45	0.011	0.034	0.006		0.006
2014-08-16	21.6	5.2 / 5.1	1	226 / 86 / 168	-0.002	0.022	-0.005	0	-0.005
			2	317 / 78 / 5	-0.002	0.002	-0.002		-0.002

5.3 Coulomb Stress Changes on Faults and beneath the Head Area of Xiluodu Reservoir

The fault geometry and orientation influence the estimation of stress changes. However, this information is lacking for the faults in the study area. We resolve the stress changes on all relevant faults corresponding to either thrust faulting or strike-slip faulting (Figure 9). The rake angles are set to be 90º for thrust faulting, 0º and 180º for left-lateral (EJF, MYF, and JMF) and right-lateral (HLF) strike-slip faulting, respectively. The dip angles at depth are set to be constant and the same as those in the pore pressure diffusion model. The estimated ΔCFS_s corresponds to the maximum water level change of 160 m without considering the dissipation of undrained pore pressure, representing an upper bound of the plausible values. The results show that the $\Delta\sigma_n$ due to reservoir load significantly increases on fault segments near the reservoir, gradually decreases to negative, and finally diminishes at a larger distance (Figure 9). In the case of thrust faulting, the $\Delta\tau$ significantly increases on the southern segment of the EJF and the southwestern segment of the HLF adjacent to the reservoir, consequently leading to the positive ΔCFS_s. While the estimations of ΔCFS_s of the JMF and MYF are relatively small, we note that the water load tends to induce the positive ΔCFS_s at the southern segment of the JMF within 2 km depth and the middle segment of MYF, coinciding with most of the events near these two faults. This means that the stress changes due to water load can contribute to the reactivation of JMF and MYF, and consequently those events nearby. In the case of strike-slip faulting, positive values of $\Delta\tau$ are only present in a few local segments at the shallow depth and tend to induce the negative ΔCFS_s on faults. This suggests that the stress changes induced by the reservoir load are inclined to promote the thrust-slip motion of the EJF and HLF segments and suppress the strike-slip motion there. We also compute the ΔCFS_p corresponding to the pore pressure diffusion on faults for case B on October 1, 2014, when the first time that water level reached its historical high. As shown in Figure 9, the maximum positive ΔCFS_s on fault segments corresponds to the thrust faulting and are generally less than 0.01 MPa. In comparison, the ΔCFS_p could exceed 0.01 MPa on most segments of the HLF and approximately half of the EJF adjacent to the reservoir.

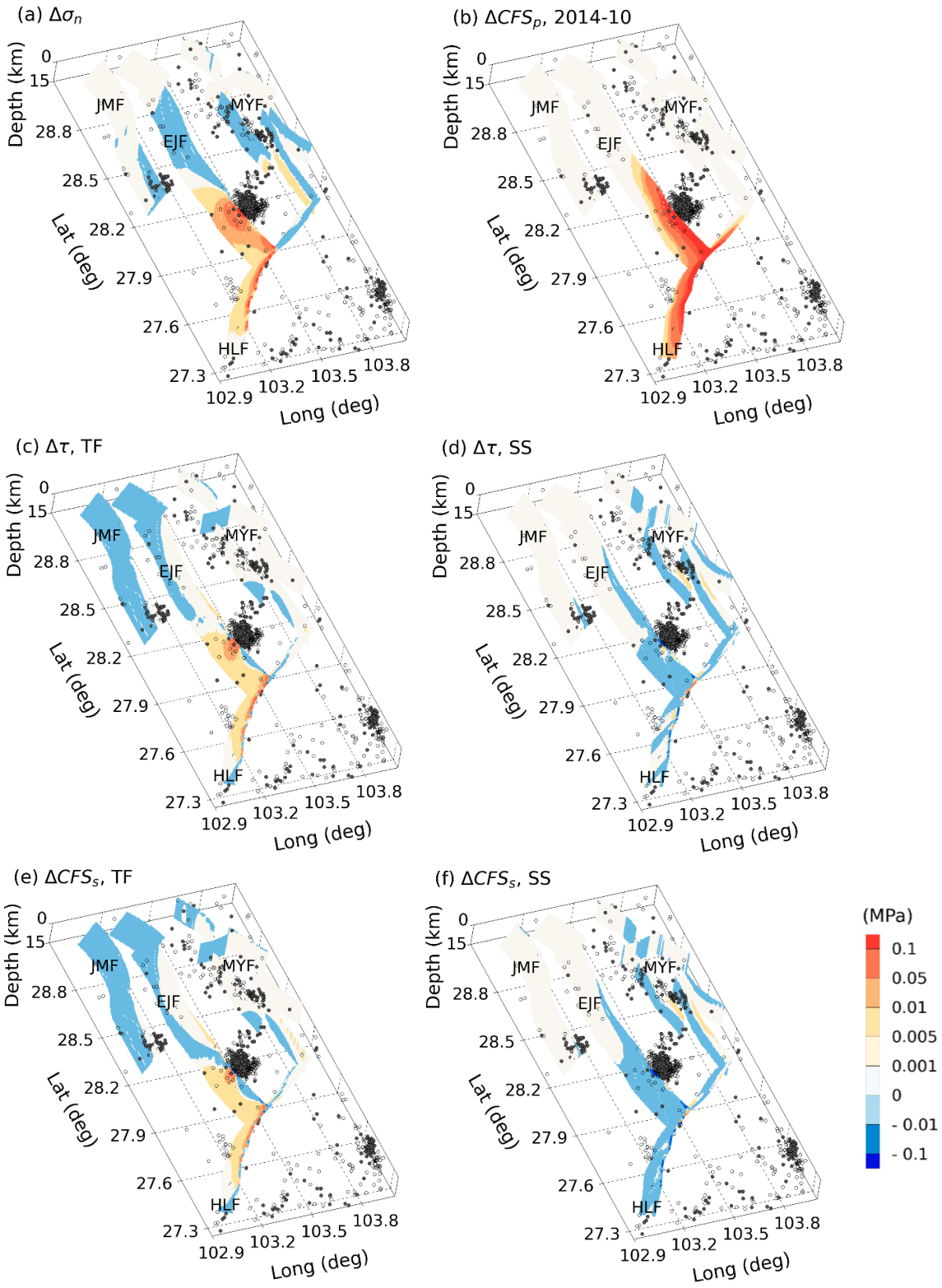

Figure 9. Shear stress, normal stress, and Coulomb stress change resulting from reservoir load (ΔCFS_s), and Coulomb stress changes resulting from pore pressure diffusion (ΔCFS_p, on October 10, 2014, for case B) on faults. The scenario of thrust faulting (TF) and strike-slip faulting (SS)

were both considered. The hypocenters of M1+ earthquakes recorded from May 2013 to June 2015 and from July 2015 to January 2020 are shown as filled and open black circles, respectively.

We also resolve the Coulomb stress changes in the head area of the reservoir, where most events are located immediately following the impoundment. Although there are no major faults in the head area of the XLD reservoir, focal mechanism solutions of events nearby (Duan, 2019) suggest the existence of NE-striking faults. Therefore, we suspect that there are unmapped faults sub-parallel to the HLF and modeled so, that is, with an average strike and dip angles of 235º and 60º, respectively. We compute the stress changes induced by reservoir load for both thrust and right-lateral strike-slip faulting, corresponding to rake angles of 90º and 180º, respectively (Figure S14). Figure 10 shows the seismicity cloud following the impoundment overlaid by the ΔCFS_s corresponding to the maximum water level change of 160 m, and ΔCFS_p on October 1, 2014, for case B. For each reference mapview plane considered in Figure 10, the events within $\pm$ 1 km depth are included for comparison. The distribution of ΔCFS_s and ΔCFS_p correlate well with the shape of the reservoir at shallow depth and vary as the depth increases. In the case of thrust faulting, the ΔCFS_s is at its maximum value of more than 0.1 MPa at shallow depth, and the positive ΔCFS_s area spatially expands as depth increases. Due to the significant increase of $\Delta\tau$ beneath the reservoir, the ΔCFS_s can reach about 0.01 MPa at 15 km depth, which is unlikely for pore pressure diffusion to reach, especially shortly after the initial impoundment. In the case of strike-slip faulting, the signs of the calculated values of ΔCFS_s are opposite to those of thrust faulting. The area with modeled ΔCFS_p values $\geq$ 0.005 MPa overlaps with most events within 12 km depth as of October 2014 (case B).

In short, the reasonable correlation between the modeled stress changes and the actual earthquake locations corroborates the possible influence of reservoir impoundment on nearby seismicity. The pore pressure diffusion can be quite relevant to fault reactivation, especially at shallow depth. In comparison, the effect of reservoir load can be far-reaching and alter the fault criticality at greater depths and distances. The combination of these two effects can induce positive Coulomb stress change and contribute to the earthquake triggering both temporally and spatially. It is important to note that the spatial pattern of the ΔCFS_s is highly dependent on the fault orientation and slip directions (Deng et al., 2020; Segall & Lu, 2015). Thus, the model with more geological details could facilitate a more realistic distribution of Coulomb stress changes.

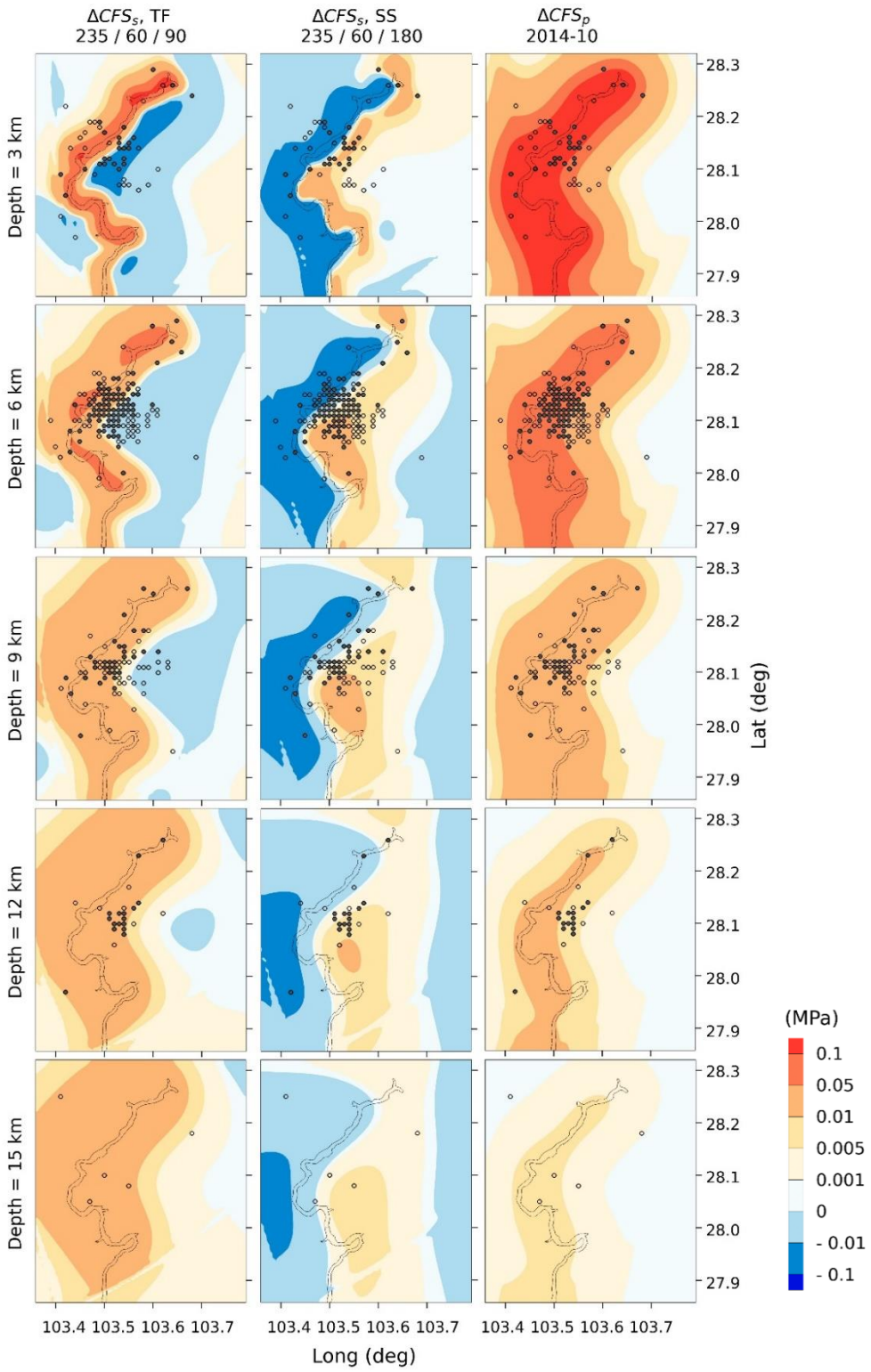

Figure 10. Spatial distribution of modeled Coulomb stress changes resulting from reservoir load (ΔCFS_s) and pore pressure diffusion (ΔCFS_p, on October 10, 2014) in the head area of the Xiluodu reservoir. The corresponding water level change ΔH_{max} = 160 m, μ = 0.71, B = 0.8. The scenarios of thrust faulting (TF) and strike-slip faulting (SS) were both considered. The M1+

earthquakes following the impoundment of the Xiluodu reservoir are shown for depth intervals within 1 km with respect to each observation plane. The M1+ events observed from May 2013 to June 2015 and from July 2015 to January 2020 are shown as filled and open black circles, respectively.

6 Concluding Remarks

There has been increasing concern over the construction of four hydropower stations situated along the Jinsha River, due to the dramatically increased seismicity following the impoundment of Xiluodu and Xiangjiaba reservoirs. This calls for an in-depth analysis of the temporal and spatial correlation between seismicity and the impoundment-induced stress and pore pressure changes. In this paper, we first conducted a fault criticality analysis in the areas of the four hydropower stations as a first-order quantification of the proximity of faults to slip. Based on the calculation of fault instability *I*, we conclude that the NNW- and NS- striking faults are more critical in this region, and the faults near the Wudongde and Baihetan dams are more likely to be reactivated than those near the Xiluodu dam. This indicates an even larger seismic risk near the Wudongde and Baihetan reservoirs. Then, we take the Xiluodu reservoir, with detailed records of water level changes and seismicity, as a timely example to study the impact of reservoir impoundment on regional seismicity. The spatio-temporal pattern of seismicity near the Xiluodu reservoir and nearby faults suggests a positive correlation with the impoundment, revealing both rapid and delayed seismic response to water level changes.

To quantify the effect of the Xiluodu reservoir impoundment on the regional seismicity, we compute the changes of pore pressure, stress, and the resulting Coulomb stress due to pore pressure diffusion and reservoir water load. Our pore pressure modeling shows that the spatial extent of elevated pore pressure expands with time during the impoundment, and the hydraulic diffusivity of the basement rock and faults exert a strong influence on the diffusion process. For the hydraulic diffusivity of the basement rock of 0.05 m^2 s^{-1}, the pore pressure changes at the majority of M1+ hypocenters near the head area of the reservoir following the impoundment can exceed 0. 01 MPa, in the order of the empirical threshold to reactivate certain critically stressed fault segments. The pore pressure diffusion also appears to exhibit appreciable impact to promote the slip of the EJF and HLF directly, while with little influence on the MYF and JMF, because of their relatively long distance away from the reservoir. The results of Coulomb stress modeling indicate that the water load can promote the thrust-slip motion and suppress the strike-slip motion of faults, especially for the segments of EJF and HLF that are close to the reservoir. The water load tends to induce the small positive Coulomb stress changes at larger depths and distances, for example, near the southern segment of the JMF and the middle segment of the MYF, which are about 30 km and 10 km from the reservoir, respectively, and are not realistic for pore pressure diffusion to reach at the time of the events. In the head area of the reservoir, the extent of positive Coulomb stress changes varies with depth, basically covering the majority of the M1+ events given thrust faulting stress environment. The pore pressure diffusion contributes to the positive Coulomb stress changes at the shallower depth, and gradually decreases at greater depth. At deeper depth, for example, at 12 and 15 km depth, the upper bound of extent where $\Delta CFS_s \geq 0.01$ MPa, is even larger than the extent where $\Delta CFS_p \geq 0.01$ MPa when the first time water level reached maximum water level change of 160 m in October 2014. In short, it can be expected that the pore pressure diffusion can continuously increase the Coulomb stress changes in future operations of the Xiluodu reservoir until reaching a regional hydrological steady state; in contrast, the contribution of reservoir load to positive Coulomb stress changes will decrease

with time due to undrained pore pressure dissipation. Further simulation with emphasis on the coupled poroelastic effect is required.

We also attempt to integrate the spatio-temporal distribution of seismicity, modeled pore pressure and stress changes in the XLD area, and fault criticality quantification. The calculated Coulomb stress changes due to pore pressure diffusion and reservoir water load are significant beneath the head area of the Xiluodu reservoir and near the EJF, which agrees with the significant seismicity increase following the impoundment. The modeled Coulomb stress changes are most significant on the HLF due to proximity to the reservoir; however, the HLF does not feature stronger seismicity than the other three faults. This observation corroborates the fault criticality analysis that the NE-striking faults (such as the HLF) are less critically-stressed than the NNW- and NS-striking faults downstream the Jinsha River. Moreover, the significant seismicity increase near the MYF contrasts the relatively small Coulomb stress changes simulated on the MYF. This observation is consistent with the fault criticality analysis, as the MYF is quantified as being more critically-stressed. Another possible influence factor on the seismicity increase near the MYF: the MYF is located upstream of the previously impounded Xiangjiaba reservoir (started from October 2012), which might also induce considerable hydro-mechanical influence on the MYF. This is out of the scope of this paper but warrants further study. Besides, the seismicity clustered at the southern end of the JMF indicates that the fault is critically stressed, contradicting the fact that the fault criticality analysis has identified the JMF as more stable in the prevailing stress field. This inconsistency may be due to the local variations of the in-situ stress field or the uncertainty of the assumed fault dip angles, which warrants further investigation. Our modeling results show that the probability of pore pressure diffusion reaching the southern end of the JMF is low, whilst the reservoir load tends to slightly increase the Coulomb stress on the southern end of the JMF and might contribute to the earthquake triggering.

To conclude, our study provides a useful and timely analysis of how reservoir impoundment can affect fault criticality and regional seismicity from the perspective of hydro-mechanical changes. More information on the geomechanical and hydro-mechanical parameters and regional faults is required to bring about further analysis. The case study of the Xiluodu reservoir has important implications, especially for Wudongde and Baihetan hydropower stations which are close to faults of presumably higher criticality, according to our analysis. The future impoundment operations there demand careful considerations and in-depth research, as well as forward-looking mitigation measures.

Acknowledgments, Samples, and Data

This research was supported by the National Natural Science Foundation of China under Project No. 51739006 and the State Key Laboratory of Hydroscience and Hydraulic Engineering under Grant No. 2019-KY-03. Acknowledgment for the data support from ‘China Earthquake Networks Center, National Earthquake Data Center. (http://data.earthquake.cn)’ and ‘ISC Bulletin: Focal mechanism search. (http://www.isc.ac.uk/iscbulletin/search/fmechanisms/)’. The support provided by the China Scholarship Council (CSC) during the visit of Man Zhang to ETH Zurich is greatly appreciated. X. Ma acknowledges the funding from Swiss National Science Foundation (Grant No. 182150) and ETH Zürich Research Grant (No. ETH-06 19-1). S. Ge

acknowledges the visiting professorship from ETH Zürich Department of Earth Sciences and the Geothermal Energy and GeoFluids Group.

References

Bell, M. L., & Nur, A. (1978). Strength changes due to reservoir-induced pore pressure and stresses and application to Lake Oroville. *Journal of Geophysical Research, 83*(NB9), 4469-4483. doi:10.1029/JB083iB09p04469

Biot, M. A. (1956). General solutions of the equations of elasticity and consolidation for a porous material. *Journal of Applied Mechanics, 78*, 91-96.

Blanpied, M. L., Lockner, D. A., & Byerlee, J. D. (1995). Frictional slip of granite at hydrothermal conditions. *Journal of Geophysical Research-Solid Earth, 100*(B7), 13045-13064. doi:10.1029/95jb00862

Brown, M. R. M., & Ge, S. (2018). Small earthquakes matter in injection-induced seismicity. *Geophysical Research Letters, 45*(11), 5445-5453. doi:10.1029/2018gl077472

Brown, M. R. M., Ge, S., Sheehan, A. F., & Nakai, J. S. (2017). Evaluating the effectiveness of induced seismicity mitigation: Numerical modeling of wastewater injection near Greeley, Colorado. *Journal of Geophysical Research-Solid Earth, 122*(8), 6569-6582. doi:10.1002/2017jb014456

Brudy, M., Zoback, M. D., Fuchs, K., Rummel, F., & Baumgartner, J. (1997). Estimation of the complete stress tensor to 8 km depth in the KTB scientific drill holes: Implications for crustal strength. *Journal of Geophysical Research-Solid Earth, 102(*B8), 18453-18475. doi:10.1029/96jb02942

Carder, D. S. (1945). Seismic investigations in the Boulder Dam area, 1940-1944, and the influence of reservoir loading on local earthquake activity*. *Bulletin of the Seismological Society of America, 35*(4), 175-192.

Cheng, A. H.-D. (2016). *Poroelasticity* (Vol. 27). Switzerland: Springer International Publishing. doi:10.1007/978-3-319-25202-5

Cocco, M., & Rice, J. R. (2002). Pore pressure and poroelasticity effects in Coulomb stress analysis of earthquake interactions. *Journal of Geophysical Research,* 107(B2), ESE2-1-2-17.

Cochran, E. S., Vidale, J. E., & Tanaka, S. (2004). Earth tides can trigger shallow thrust fault earthquakes. *Science, 306*(5699), 1164-1166. doi:10.1126/science.1103961

Cui, X., Xie, F., & Zhang, H. (2006). Recent tectonic stress field zoning in Sichuan-Yunnan region and its dynamic interest. *Acta Seismologica Sinica, 28*(5), 451-461. (in Chinese)

Cui, Y., Deng, J., & Xu, C. (2019). The activity of the Yaziba Fault on the lower reaches of the Jinsha River, Southwestern China: indirect evidence from Paleo earthquakes and ancient landslides. *Advances in Civil Engineering, 2019*. doi:10.1155/2019/5020357

Deng, K., Liu, Y., & Chen, X. (2020). Correlation between poroelastic stress perturbation and multidisposal wells induced earthquake sequence in cushing, Oklahoma. *Geophysical Research Letters, 47*(20), e2020GL089366. doi:10.1029/2020GL089366

Diao, G., Wang, Y., Feng, X., Wang, X., Feng, Z., Zhang, H., et al. (2014). Analysis of characteristics of focal mechanism in reservoir head region of Xiluodu reservoir after impoundment. *Seismology and Geology, 36*(3), 644-657. (in Chinese)

Duan, M. (2019). *Study on characteristics of focal mechanisms and stress field in the downstream reservoir area of Jinsha River.* (Master's thesis), Institude of Earthquake Forecasting, CEA. Available from https://kns.cnki.net/KCMS/detail/detail.aspx?dbname=CMFD201902&filename=1019066558.nh (in Chinese)

El Hariri, M., Abercrombie, R. E., Rowe, C. A., & do Nascimento, A. F. (2010). The role of fluids in triggering earthquakes: observations from reservoir induced seismicity in Brazil. *Geophysical Journal International, 181*(3), 1566-1574. doi:10.1111/j.1365-246X.2010.04554.x

Gao, H., Zhang, D., Lu, J., Yin, G., & Wu, M. (2020). Experimental study on influence of intermediate principal stress on the permeability of sandstone. *Transport in Porous Media, 135*(3), 753-778. doi:10.1007/s11242-020-01500-2

Gavrilenko, P., & Gueguen, Y. (1989). Pressure dependence of permeability: a model for cracked rocks. *Geophysical Journal International, 98*(1), 159-172. doi:10.1111/j.1365-246X.1989.tb05521.x

Ge, S., Liu, M., Lu, N., Godt, J. W., & Luo, G. (2009). Did the Zipingpu Reservoir trigger the 2008 Wenchuan earthquake? *Geophysical Research Letters, 36*. doi:10.1029/2009gl040349

Gephart, J. W., & Forsyth, D. W. (1984). An improved method for determining the regional stress tensor using earthquake focal mechanism data: Application to the San Fernando Earthquake Sequence. *Journal of Geophysical Research, 89*(NB11), 9305-9320. doi:10.1029/JB089iB11p09305

Goebel, T. H. W., Weingarten, M., Chen, X., Haffener, J., & Brodsky, E. E. (2017). The 2016 Mw5.1 Fairview, Oklahoma earthquakes: Evidence for long-range poroelastic triggering at > 40 km from fluid disposal wells. *Earth and Planetary Science Letters, 472*, 50-61. doi:10.1016/j.epsl.2017.05.011

Guglielmi, Y., Cappa, F., Avouac, J.-P., Henry, P., & Elsworth, D. (2015). Seismicity triggered by fluid injection-induced aseismic slip. *Science, 348*(6240), 1224-1226. doi:10.1126/science.aab0476

Gupta, H. K. (1985). The present status of reservoir induced seismicity investigations with special emphasis on Koyna earthquakes. *Tectonophysics, 118*(3-4), 257-279. doi:10.1016/0040-1951(85)90125-8

Gupta, H. K. (1992). Reservoir-induced earthquakes. *Current Science, 62*(1-2), 183-198.

Gupta, H. K. (2002). A review of recent studies of triggered earthquakes by artificial water reservoirs with special emphasis on earthquakes in Koyna, India. *Earth-Science Reviews, 58*(3-4), 279-310. doi:10.1016/s0012-8252(02)00063-6

Harbaugh, A. W. (2005). *MODFLOW-2005, the U.S. Geological Survey modular ground-water model -- the Ground-Water Flow Process: U.S. Geological Survey Techniques and Methods 6-A16*: US Department of the Interior, US Geological Survey Reston, VA.

Harbaugh, A. W., Langevin, C. D., Hughes, J. D., Niswonger, R. N., & Konikow, L. F. (2017). MODFLOW-2005 Version 1.12. 00, the U.S. Geological Survey modular groundwater model: U.S. Geological Survey Software Release, 03 February 2017. doi:10.5066/F7RF5S7G

Harris, R. A. (1998). Introduction to special section: stress triggers, stress shadows, and implications for seismic hazard. *Journal of Geophysical Research-Solid Earth, 103*(B10), 24347-24358. doi:10.1029/98jb01576

Heidbach, O., Rajabi, M., Cui, X., Fuchs, K., Müller, B., Reinecker, J., et al. (2018). The World Stress Map database release 2016: Crustal stress pattern across scales. *Tectonophysics, 744*, 484-498. doi:10.1016/j.tecto.2018.07.007

Heidbach, O., Rajabi, M., Reiter, K., Ziegler, M., & Team, W. S. M. (2016). World Stress Map Database Release 2016. *GFZ German Research Centre for Geosciences*. doi:10.5880/WSM.2016.001

Heller, R., Vermylen, J., & Zoback, M. (2014). Experimental investigation of matrix permeability of gas shales. *Aapg Bulletin, 98*(5), 975-995. doi:10.1306/09231313023

Hu, X., Zang, A., Heidbach, O., Cui, X., Xie, F., & Chen, J. (2017). Crustal stress pattern in China and its adjacent areas. *Journal of Asian Earth Sciences, 149*, 20-28. doi:10.1016/j.jseaes.2017.07.005

Ingebritsen, S. E., & Manning, C. E. (1999). Geological implications of a permeability-depth curve for the continental crust. *Geology, 27*(12), 1107-1110. doi:10.1130/0091-7613(1999)027<1107:Gioapd>2.3.Co;2

Itasca Consulting Group, Inc. (2012). FLAC3D–fast Lagrangian analysis of continua in three-dimensions, Ver. 5.0. Minneapolis: Itasca.

Jin, H., Gao, Y., Su, X., & Fu, G. (2019). Contemporary crustal tectonic movement in the southern Sichuan-Yunnan block based on dense GPS observation data. *Earth and Planetary Physics, 3*(1), 53-61. doi:10.26464/epp2019006

King, G. C. P., Stein, R. S., & Lin, J. (1994). Static stress changes and the triggering of earthquakes. *Bulletin of the Seismological Society of America, 84*(3), 935-953.

Lamontagne, M., Hammamji, Y., Tournier, J. P., & Woodgold, C. (2006). Reservoir-induced earthquakes at Sainte-Marguerite-3, Quebec, Canada. *Canadian Journal of Earth Sciences, 43*(2), 135-146. doi:10.1139/e05-108

Luo, J., Li, Y., & Ye, J. (2020). Seismic activity analysis in the Xiluodu Reservoir affected area. *Journal of Seismological Research, 43*(1), 118-124. (in Chinese)

Masuda, K., Arai, T., Fujimoto, K., Takahashi, M., & Shigematsu, N. (2012). Effect of water on weakening preceding rupture of laboratory-scale faults: Implications for long-term weakening of crustal faults. *Geophysical Research Letters, 39*. doi:10.1029/2011gl050493

Ortiz, J. P., Person, M. A., Mozley, P. S., Evans, J. P., & Bilek, S. L. (2019). The role of fault-zone architectural elements on pore pressure propagation and induced seismicity. *Groundwater, 57*(3), 465-478. doi:10.1111/gwat.12818

Pan, Y., & Shen, W.-B. (2017). Contemporary crustal movement of southeastern Tibet: Constraints from dense GPS measurements. *Scientific Reports, 7*. doi:10.1038/srep45348

Pandey, A. P., & Chadha, R. K. (2003). Surface loading and triggered earthquakes in the Koyna-Warna region, western India. *Physics of the Earth and Planetary Interiors, 139*(3-4), 207-223. doi:10.1016/j.pepi.2003.08.003

Rajendran, K., & Talwani, P. (1992). The role of elastic, undrained, and drained responses in triggering earthquakes at Monticello Reservoir, South-Carolina. *Bulletin of the Seismological Society of America, 82*(4), 1867-1888.

Raleigh, C. B., Healy, J. H., & Bredehoeft, J. D. (1976). Experiment in earthquake control at Rangely, Colorado. *Science, 191*(4233), 1230-1237. doi:10.1126/science.191.4233.1230

Reasenberg, P. A., & Simpson, R. W. (1992). Response of regional seismicity to the static stress change produced by the Loma-Prieta earthquake. *Science, 255*(5052), 1687-1690. doi:10.1126/science.255.5052.1687

Robinson, R. (2004). Potential earthquake triggering in a complex fault network: the northern South Island, New Zealand. *Geophysical Journal International, 159*(2), 734-748. doi:10.1111/j.1365-246X.2004.02446.x

Roeloffs, E. A. (1988). Fault stability changes induced beneath a reservoir with cyclic variations in water level. *Journal of Geophysical Research-Solid Earth and Planets, 93*(B3), 2107-2124. doi:10.1029/JB093iB03p02107

Ruiz-Barajas, S., Santoyo, M. A., Benito Oterino, M. B., Alvarado, G. E., & Climent, A. (2019). Stress transfer patterns and local seismicity related to reservoir water-level variations. A case study in central Costa Rica. *Scientific Reports, 9*. doi:10.1038/s41598-019-41890-y

Segall, P., Grasso, J. R., & Mossop, A. (1994). Poroelastic stressing and induced seismicity near the Lacq gas field, southwestern France. *Journal of Geophysical Research-Solid Earth, 99*(B8), 15423-15438. doi:10.1029/94jb00989

Segall, P., & Lu, S. (2015). Injection-induced seismicity: poroelastic and earthquake nucleation effects. *Journal of Geophysical Research-Solid Earth, 120*(7), 5082-5103. doi:10.1002/2015jb012060

Shen, L. W., Schmitt, D. R., & Schultz, R. (2019). Frictional stabilities on induced earthquake fault planes at Fox Creek, Alberta: a pore fluid pressure dilemma. *Geophysical Research Letters, 46*(15), 8753-8762. doi:10.1029/2019gl083566

Simpson, D. W. (1976). Seismicity changes associated with reservoir loading. *Engineering Geology, 10*(2-4), 123-150. doi:10.1016/0013-7952(76)90016-8

Simpson, D. W., Leith, W. S., & Scholz, C. H. (1988). Two types of reservoir-induced seismicity. *Bulletin of the Seismological Society of America, 78*(6), 2025-2040.

Snee, J. E. L., & Zoback, M. D. (2018). State of stress in the Permian Basin, Texas and New Mexico: implications for induced seismicity. *Leading Edge, 37*(2), 127-134. doi:10.1190/tle37020127.1

Stabile, T. A., Giocoli, A., Lapenna, V., Perrone, A., Piscitelli, S., & Telesca, L. (2014). Evidence of low-magnitude continued reservoir-induced seismicity associated with the Pertusillo Artificial Lake (Southern Italy). *Bulletin of the Seismological Society of America, 104*(4), 1820-1828. doi:10.1785/0120130333

Stein, R. S. (1999). The role of stress transfer in earthquake occurrence. *Nature, 402*(6762), 605-609. doi:10.1038/45144

Sumy, D. F., Cochran, E. S., Keranen, K. M., Wei, M., & Abers, G. A. (2014). Observations of static Coulomb stress triggering of the November 2011 M5.7 Oklahoma earthquake sequence. *Journal of Geophysical Research-Solid Earth, 119*(3), 1904-1923. doi:10.1002/2013jb010612

Talwani, P. (1997). On the nature of reservoir-induced seismicity. *Pure and Applied Geophysics, 150*(3-4), 473-492. doi:10.1007/s000240050089

Talwani, P. (2000). Seismogenic properties of the crust inferred from recent studies of reservoir-induced seismicity - Application to Koyna. *Current Science, 79*(9), 1327-1333.

Talwani, P., & Acree, S. (1984). Pore pressure diffusion and the mechanism of reservoir-induced seismicity. *Pure and Applied Geophysics, 122*(6), 947-965.

Talwani, P., Chen, L., & Gahalaut, K. (2007). Seismogenic permeability, k(s). *Journal of Geophysical Research-Solid Earth, 112*(B7). doi:10.1029/2006jb004665

Tao, W., Masterlark, T., Shen, Z.-K., & Ronchin, E. (2015). Impoundment of the Zipingpu reservoir and triggering of the 2008 M-w 7.9 Wenchuan earthquake, China. *Journal of Geophysical Research-Solid Earth, 120*(10), 7033-7047. doi:10.1002/2014jb011766

Tian, J., Luo, Y., & Zhao, L. (2019). Regional stress field in Yunnan revealed by the focal mechanisms of moderate and small earthquake. *Earth and Planetary Physics, 3*(3), 243-252. doi:10.26464/epp2019024

Vavrycuk, V. (2014). Iterative joint inversion for stress and fault orientations from focal mechanisms. *Geophysical Journal International, 199*(1), 69-77. doi:10.1093/gji/ggu224

Vavrycuk, V., Bouchaala, F., & Fischer, T. (2013). High-resolution fault image from accurate locations and focal mechanisms of the 2008 swarm earthquakes in West Bohemia, Czech Republic. *Tectonophysics, 590*, 189-195. doi:10.1016/j.tecto.2013.01.025

Walsh, F. R., III, & Zoback, M. D. (2016). Probabilistic assessment of potential fault slip related to injection-induced earthquakes: Application to north-central Oklahoma, USA. *Geology, 44*(12), 991-994. doi:10.1130/g38275.1

Wang, Z., Zhao, D., & Wang, J. (2010). Deep structure and seismogenesis of the north-south seismic zone in Southwest China. *Journal of Geophysical Research-Solid Earth, 115*. doi:10.1029/2010jb007797

Wen, X., Du, F., Yi, G., Long, F., Fan, J., Yang, P., et al. (2013). Earthquake potential of the Zhaotong and Lianfeng fault zones of the eastern Sichuan-Yunnan border region. *Chinese Journal of Geophysics-Chinese Edition, 56*(10), 3361-3372. doi:10.6038/cjg20131012 (in Chinese)

Wetzler, N., Shalev, E., Gobel, T., Amelung, F., Kurzon, I., Lyakhovsky, V., & Brodsky, E. E. (2019). Earthquake swarms triggered by groundwater extraction near the Dead Sea Fault. *Geophysical Research Letters, 46*(14), 8056-8063. doi:10.1029/2019gl083491

Xu, Z., Huang, Z., Wang, L., Xu, M., Ding, Z., Wang, P., et al. (2016). Crustal stress field in Yunnan: implication for crust-mantle coupling. *Earthquake Science, 29*(2), 105-115. doi:10.1007/s11589-016-0146-3

Xuan, S., Shen, C., Li, H., & Tan, H. (2016). Structural interpretation of the Chuan-Dian block and surrounding regions using discrete wavelet transform. *International Journal of Earth Sciences, 105*(5), 1591-1602. doi:10.1007/s00531-015-1272-1

Yang, L., Li, B., & Chang, T. (2019). Seismicity characteristics of Xiangjiaba Reservoir region before and after the impoundment. *Journal of Geodesy and Geodynamics, 39*(9), 919-923. (in Chinese)

Yeo, I. W., Brown, M. R. M., Ge, S., & Lee, K. K. (2020). Causal mechanism of injection-induced earthquakes through the M-w 5.5 Pohang earthquake case study. *Nature Communications, 11*(1). doi:10.1038/s41467-020-16408-0

Yin, Y., Huang, B., Wang, S., & Li, J. (2015). Potential for a ganhaizi landslide-generated surge in Xiluodu Reservoir, Jinsha River, China. *Environmental Earth Sciences, 73*(7), 3187-3196. doi:10.1007/s12665-014-3619-5

Zhang, L., Li, J., Sun, X., Liao, W., Zhao, Y., Wei, G., & He, C. (2018). A possible mechanism of reservoir-induced earthquakes in the Three Gorges Reservoir, Central China. *Bulletin of the Seismological Society of America, 108*(5B), 3016-3028. doi:10.1785/0120180015

Zhang, Y., Person, M., Rupp, J., Ellett, K., Celia, M.A., Gable, C.W., Bowen, B., Evans, J., Bandilla, K., Mozley, P., Dewers, T. and Elliot, T. (2013). Hydrogeologic controls on induced seismicity in crystalline basement rocks due to fluid injection into Basal Reservoirs. *Ground Water, 51*(4), 525-538. doi:10.1111/gwat.12071

Zhu, D.-C., Wang, Q., Cawood, P. A., Zhao, Z.-D., & Mo, X.-X. (2017). Raising the Gangdese Mountains in southern Tibet. *Journal of Geophysical Research-Solid Earth, 122*(1), 214-223. doi:10.1002/2016jb013508

Zoback, M. D. (2007). *Reservoir geomechanics*. Cambridge, UK: Cambridge University Press. doi:10.1017/CBO9780511586477

Zoback, M. D., & Healy, J. H. (1984). Friction, faulting and in-situ stress. *Annales Geophysicae, 2*(6), 689-698.

Zoback, M. D., Townend, J., & Grollimund, B. (2002). Steady-state failure equilibrium and deformation of intraplate lithosphere. *International Geology Review, 44*(5), 383-401. doi:10.2747/0020-6814.44.5.383